

# Optical properties of circular Bragg gratings in labyrinth geometry

Quirin Buchinger<sup>\*1</sup>, Simon Betzold<sup>1</sup>, Sven Höfling<sup>1</sup>, and Tobias Huber-Loyola<sup>1</sup>

<sup>1</sup>Lehrstuhl für Technische Physik, Universität Würzburg, Würzburg, Germany

## Abstract:

We present an optical study of new device designs for electrically contactable circular Bragg grating cavities in labyrinth geometries. We propose to rotate the connections between adjacent rings to disable waveguiding and improve the mode confinement. To find the optimal design, six different layouts with either 3-fold or 4-fold symmetry and one with 2-fold symmetry are investigated experimentally and numerically. Measurements show that increasing the connection width has a different impact on device performance, depending on the arrangement of the connections between consecutive rings. We compare results between different layouts and performed polarization dependent measurements to investigate whether the connections create asymmetries in the photonic confinement that would impede the performance of the device.

Semiconductor quantum dots (QDs) are promising sources for single or entangled photons for use in quantum cryptography [1,2] and optical quantum computing [3]. They benefit from high brightness and indistinguishability [4,5]. To enhance their performance, they are typically embedded in microcavities. Recently, the circular Bragg grating resonator [6] has gained a lot of attention as a cavity to embed semiconductor quantum dots [7-11]. This attention comes from fast growth, compared with resonators that rely on vertical distributed Bragg reflectors, like micropillar resonators [4,5], and its high Purcell enhancement in a broad frequency range. This enables Purcell enhancement of both the biexciton and exciton emission simultaneously [7,11], which required complicated photonic molecules before [12]. However, various applications, like a blinking free operation, deterministic charging [13] or switching of quantum dot molecules [14], require embedding the quantum emitters in a diode structure with electrical contacts on the device. Early device geometries, which were not completely etched [8], would allow for a bottom contact, but a top contact still seems out of reach. Furthermore, these not fully etched devices come along with a compromise in device performance, compared to devices on oxide with fully etched rings. The attempt to leave narrow waveguide-like connections is a possibility, which was already reported [15]. However, in Ref. [15] the authors report a very large device with Q factors of  $\approx 1070$ , to minimize the effect of the connection of the circular rings. Also, the connection has to be extremely narrow to not create a waveguide towards the side. Quantum dot emission coupling to the waveguide is lost for off-chip experiments.

Here, we approach this challenge by shifting the position of the connections between consecutive rings. We investigate seven different layouts for the connection positions, which have 2-fold, 3-fold or 4-fold geometry as shown and named in Figure 1 a). These layouts are compared to a bridgeless circular Bragg grating (CBG). The 4-WG (**w**aveguide) (3-WG) layouts have four (three) connections per ring, arranged in a straight line, connecting all rings in a waveguide-like fashion (for very thin connections, there is no existing waveguiding mode). The connections are distributed evenly along one ring for all layouts, resulting in always 90° (120°) offset. At the 4-LW (**l**ong **w**ay) (3-LW) layouts the connections are rotated 45° (60°) from one gap to the next. This results in a labyrinth like pattern and into a long way for applied current. To reduce this way in the 4-SW (**s**hort **w**ay) (3-SW) layouts, see Figure 1 b),

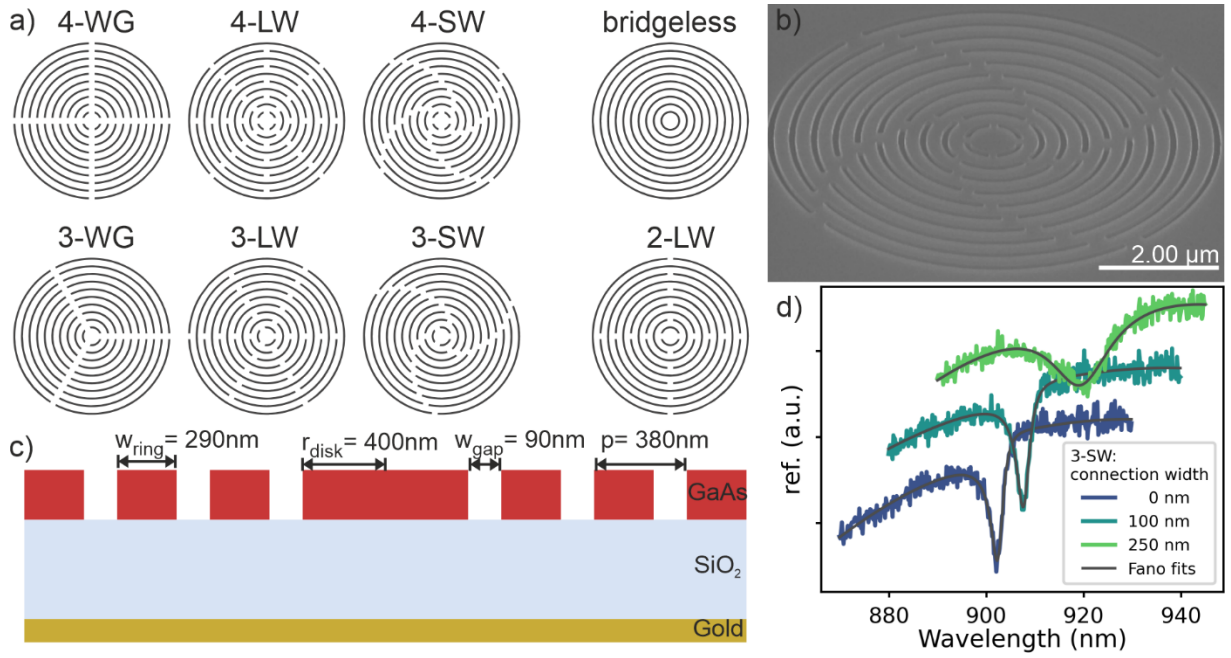


Figure 1 a) We investigated seven different layouts in comparison to a bridgeless CBG. Three layouts with four (three) connections per ring in 3 different configurations and one with two connections per ring. The layouts are named according to the number of connections per ring and the arrangement of the bridges: wave guide (WG): straight-line over all rings; long way (LW): connection position rotated by 45° (60°) from one to the next ring; and short way (SW): from the second ring outwards with small rotations. Here, the layouts are shown with a connection size of 300 nm. For the LW and SW layouts the labyrinth like structure is recognizable. b) SEM picture of CBR with 4-SW layout. c) Sketch of CBG cross-section on top of SiO<sub>2</sub>-layer and backside gold mirror. d) Exemplary reflectivity spectra of 3-SW CBGs with 0 nm, 100 nm and 250 nm connections plotted with an offset in y.

the connections are rotated 45° (60°) only for the two innermost gaps and afterwards by 15° (8° from the 5<sup>th</sup> ring outwards) from one gap to the next. This results in a windmill-like pattern. Additionally, a 2-fold geometry is used, with two opposite connections per ring rotated 90° at every second gap (2-LW). For each layout, we varied the nominal width of the connection from 50 nm over 75, 100, 150, 200, 250, 300, 350, and 400 to 450 nm. In the actual devices, the connection width is (28 ± 3) nm smaller as the nominal width due to process inaccuracies. All following numbers state the nominal width. At 50 nm connection width, the process did etch into the connection, thus it is partly etched from the top.

For all the CBGs we used a (120 ± 5) nm thick GaAs membrane on top of (360 ± 10) nm of SiO<sub>2</sub> and a gold bottom mirror. The sample was produced via a flip chip process [7,10,11]. We patterned the CBGs with electron beam lithography and dry etching. The CBGs have a central disk radius of 400 nm with a periodicity of 380 nm and a gap width of 90 nm (Figure 1 c).

To investigate the CBG fundamental mode and the influence of the different layouts and connection sizes, we performed reflectivity measurements on the devices. The acquired reflectivity spectra are normalized on a reference spectrum from a silver mirror to get relative reflectivity spectra. At the cavity resonance the spectrally flat white light is coupled into the structure resulting in a drop in reflectivity (Figure 1 d). The resulting shape is given by a Fano resonance [16], which is caused by interference of the 0-dimensional CBG mode and the 2-dimensional modes of the membrane[17]. Therefore, we fit the spectra with a Fano resonance [17,18]:

$$I(\lambda) = A \frac{(p\Gamma/2 + \lambda - \lambda_{center})^2}{(\Gamma/2)^2 + (\lambda - \lambda_{center})^2}$$

with amplitude A, center wavelength  $\lambda_{center}$ , linewidth  $\Gamma$  and Fano parameter p. At p=0 the Fano resonance converges to a Lorentzian function. When fitting, we take a quadratic background into

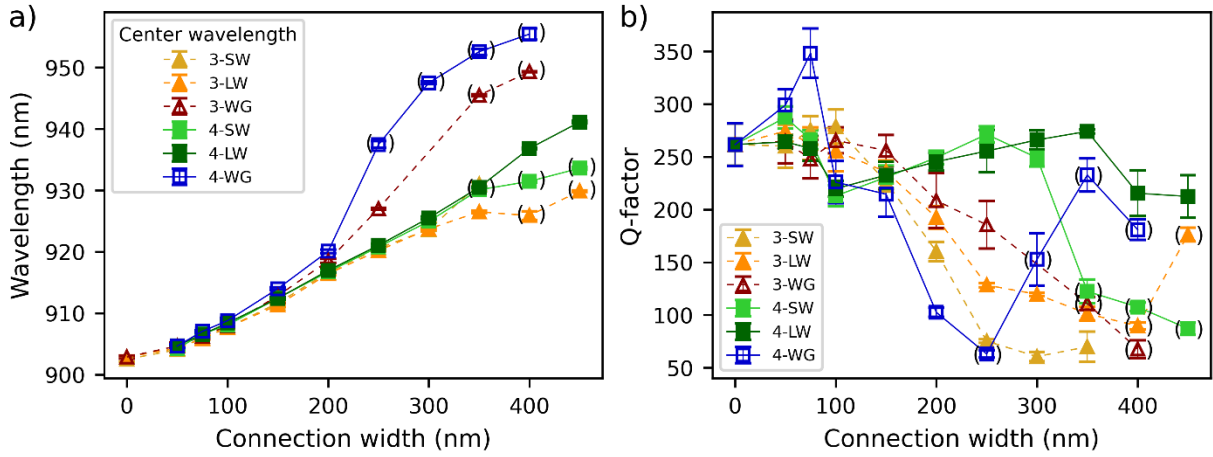


Figure 2: Effect of the connection width on wavelength and Q-factor for different layouts. Each datapoint is the mean of 5 to 6 measured devices and the error bars are the standard deviation. The excluded datapoints (marked with parentheses) represent modes which could not be clearly identified as the investigated fundamental mode (at bigger connections sometimes additional modes arise). a) Cavity resonance wavelength for the different CBG layouts in dependence of the connection width. b) Measured Q-factor for different layouts and connection widths. The Q-factors of 4-SW and 4-LW are less affected by the connections compared to all other layouts.

account, which comes from interference of planar surfaces in the structure, i.e., the upper and lower surface of the membrane. We calculate the cavity quality (Q)-factor  $Q = \lambda_{center}/FWHM$ . The FWHM is given by the full width at half the intensity between the base line and the minimum of the resonance peak from the Fano fit.

For the bridgeless CBG, the cavity resonance is determined to  $(902.51 \pm 0.39)$  nm (@4 K) with a quality factor of  $Q=262 \pm 21$  (average over 15 measured devices).

For each layout and connection size we measured several devices and calculate  $\lambda_{center}$  and the Q-factor from the fitted data. Figure 2 a) displays the center wavelength of the CBG mode in dependence of the connection size for the different layouts. For all layouts, a redshift is visible with increasing connection width. There are two processes that contribute to this redshift. First, the cavity mode is less confined in the inner disk due to the presence of the connections. Second, the effective refractive index in the structure is increased because there is more high index material present. As LW and SW show a reduced redshift compared to the wave guide layout, they have a better confinement.

Figure 2 b) shows the connection width dependence of the Q-factor. From 0 to 100 nm connection size the Q-factor for all layouts stays, within its fluctuations, the same. Afterwards it decreases for all layouts except 4-SW and 4-LW. For these two layouts changing the connection arrangement from WG to LW (SW) prevents the Q-factor from dropping. The Q-factor stays at the same level until 350 nm (300 nm). For all layouts with three connections per ring, a decrease of the Q-factor after 150 nm is observed, but the Q-factor is still higher than 4-WG.

FDTD-simulations for the different designs corroborate the results. We calculate Purcell factors  $F_p$ , far-field pattern (Figure 3 a-e) and total emission efficiencies into the upper half sphere as well as efficiencies into a given numerical aperture. For the bridgeless CBG the simulations yield a Purcell factor of 18.5 at 932 nm whereby 89.2% (thereof 90.6% into  $NA=0.64$ ) of the light is emitted upwards. For the 4-WG (250 nm bridges) the Purcell factor decreases to 12.9 (78.5 to 79% light upwards, thereof 62.3 to 58.8% into  $NA=0.64$ , depending on the dipole orientation) and more importantly, the far field pattern completely loses its Gaussian shape (Figure 3 b). Changing the layout to 4-LW (4-SW) the Purcell and the far-field pattern can be restored (Purcell factor of 18.3 (16.8 to 17.4)). For the 3-WG the Purcell factor is even lower with 8.7. Rotating the connections to 3-LW and 3-SW also restores the Purcell factor partially to 9.8 (9.7). In all 3-fold layouts the far-field patterns also strongly deviate from

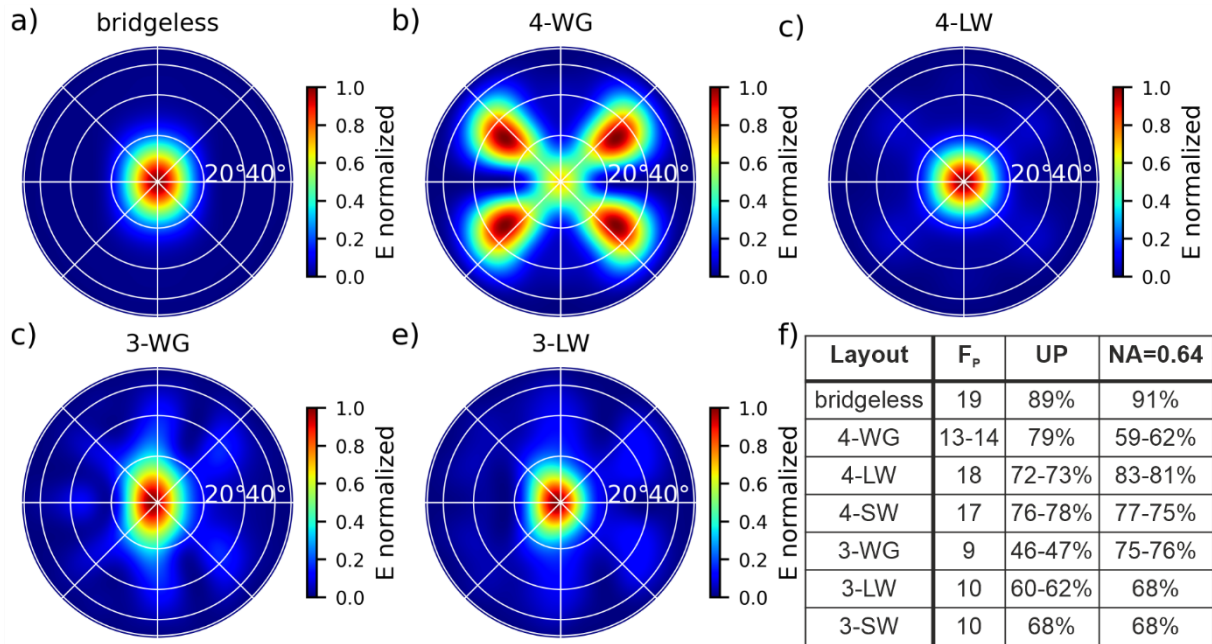


Figure 3: a)-e) Simulated far field pattern for the different layouts with a connection width of 250nm. Displayed is the electric field and not the intensity for better visibility of the small deviations. The Gaussian shape of the far field pattern of the bridgeless layout (a) is lost for 4-WG (b) and 3-WG / 3-LW (c / e). Changing the layout from 4-WG to 4-LW (c) restores the Gaussian shape. f) Simulated Purcell factor  $F_p$  and the total emission efficiencies into the upper half sphere (UP) and the fraction thereof into an NA=0.64.

a Gaussian distribution, see (Figure 3 c, e). When discussing the extraction efficiencies, we want to point out that the CBG parameters were not optimized for the new cavity wavelength. We assume that the extraction efficiencies could be increased, because we also see a non-optimal extraction efficiency for bridgeless CBGs with not optimized parameters.

### Polarization series

In a perfectly round CBG the fundamental mode consists of two perpendicularly polarized degenerate modes. This degeneracy can be lifted by introducing different confinement along different axis, like already shown in intentionally elliptical devices [19]. To investigate the effect of the introduced connections on the confinement along different directions, we performed polarization resolved reflectivity measurements. We measured three devices for each layout with connection sizes of 75 nm, 150 nm, 250 nm, and 300 nm. As reference, nine bridgeless devices were measured. The spectra are fitted with a Fano resonance. For the polarization mode splitting we evaluated the minima of the Fano resonances as the center wavelength  $\lambda_{center}$  depend on the Fano parameter  $p$  and thus do not represent the splitting correctly.

In the inlet of Figure 4 a) the wavelengths of the minima in the spectra are plotted depending on the polarization direction for one CBG without bridges. As the modes overlap severely, see Figure 4 a), we always see a superposition of the two orthogonal modes and the extrema in the sinusoidal function in Figure 4 a) inlet represent their fundamental energy. For the bridgeless CBG one would expect zero mode splitting, however, we do observe a finite splitting in most of the devices ( $(0.54 \pm 0.32)$  nm on average). This is probably caused by an anisotropic etching, which leads to a slightly elliptically CBG. Figure 4 a) displays reflectivity measurements along the H- and V-polarization.

In Figure 4 b) the polarization mode splitting of the CBGs with different layouts is shown for varying connection sizes. The splitting of all layouts with three connections per ring increases, while for four it stays the same or even decreases (4-SW and 4-LW).

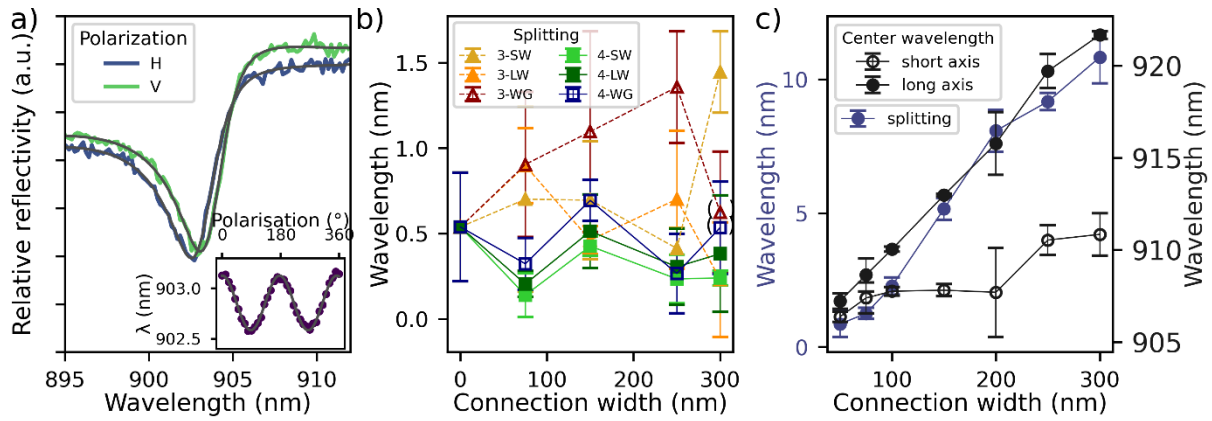


Figure 4: a) Reflectivity spectra of a bridgeless CBG along the H and V polarization. A polarization mode splitting of  $(0.541 \pm 0.009)$  nm is visible. Inlet) Minima position of the Fano resonance for different polarizations. b) Polarization mode splitting for the different CBG layouts in dependence of the connection width. For layouts with three connections per ring the splitting is increased. c) Polarization mode splitting and mode position in dependence of the connection width for the 2-LW layout. In the 2-LW layout the splitting surpasses the linewidth.

Additionally to the previously discussed designs, we also investigated a layout with only 2 connections per ring by (polarization resolved) reflectivity measurements. From one to the next gap the connections are turned by  $90^\circ$  (See Figure 1 a). By increasing the connection width, the mode splitting exceeds the cavity linewidth and thus can be seen also in polarization independent measurements. Both modes shift red with increasing connection size. The mode that is aligned along the innermost connections shifts significantly more with increasing connection width (Figure 4 c). Since the effective refractive index change of the CBG is the same for both the modes, we can conclude that the dominating effect in mode shifting is the confinement change in the central disk. This behavior is analog to the splitting observed in elliptical CBGs or micropillars [19] and offer similar application opportunities.

## Conclusion

We studied seven different layouts of electrically contactable circular Bragg grating cavities. Rotating the connections from waveguide (WG) to long-way (LW) and short-way (SW) reduces the redshift by increasing the confinement in the central disk. Comparing the influence of the connections on the Q-factor shows that layouts with four connections have a better Q-factor than three connections layouts for increasing connection widths. These results are confirmed by FDTD simulations. Furthermore, the simulations reveal that the 4-LW and 4-SW layouts preserve an almost Gaussian far field pattern. These field patterns allow good collection efficiency into single mode fibers. Layouts with three connections per ring increase the polarization mode splitting while layouts with four connections help to reduce it.

We showed a huge splitting at devices with two connections per ring. This can be used if polarized photons are required, as with elliptical devices, with the advantage of possible electrical contacts. Furthermore, by introducing connections with different sizes in layouts with four connections, this effect could help to reduce unintended mode splitting (assumed that the unintended splitting has a preferred direction, as present when introduced by anisotropic etching).

Overall, for unpolarized device performance, we suggest the 4-LW or 3-SW layout for electrical contacted CBGs. Here, 4-SW offers a layout with a shorter path length for the current if device resistance is of importance.

## Acknowledgments

We want to thank the funding agencies. Especially BMBF – Project Q.LINK.X, QR.X and Qecs (Förderkennezeichen 16KIS0871, 16KISQ010 and 13N16272), and the Deutsche

Forschungsgemeinschaft (DFG, German Research Foundation) within the projects HU2985/1-1 and HO5194/8-1 and the State of Bavaria for funding the research. Special thanks go to Silke Kuhn for processing the samples in reliable good quality.

## References

1. Lu, C.-Y. & Pan, J.-W. Quantum-dot single-photon sources for the quantum internet. *Nat. Nanotechnol.* **16**, 1294–1296; 10.1038/s41565-021-01033-9 (2021).
2. Schimpf, C. *et al.* Quantum cryptography with highly entangled photons from semiconductor quantum dots. *Science advances* **7**; 10.1126/sciadv.abe8905 (2021).
3. Raussendorf, R. & Briegel, H. J. A one-way quantum computer. *Phys. Rev. Lett.* **86**, 5188–5191; 10.1103/PhysRevLett.86.5188 (2001).
4. Somaschi, N. *et al.* Near-optimal single-photon sources in the solid state. *Nat. Photonics* **10**, 340–345; 10.1038/nphoton.2016.23 (2016).
5. Ding, X. *et al.* On-Demand Single Photons with High Extraction Efficiency and Near-Unity Indistinguishability from a Resonantly Driven Quantum Dot in a Micropillar. *Phys. Rev. Lett.* **116**, 20401; 10.1103/PhysRevLett.116.020401 (2016).
6. Scheuer, J. & Yariv, A. Coupled-waves approach to the design and analysis of bragg and photonic crystal annular resonators. *IEEE J. Quantum Electron.* **39**, 1555–1562; 10.1109/JQE.2003.819548 (2003).
7. Wang, H. *et al.* On-Demand Semiconductor Source of Entangled Photons Which Simultaneously Has High Fidelity, Efficiency, and Indistinguishability. *Phys. Rev. Lett.* **122**, 113602; 10.1103/PhysRevLett.122.113602 (2019).
8. Davanço, M., Rakher, M. T., Schuh, D., Badolato, A. & Srinivasan, K. A circular dielectric grating for vertical extraction of single quantum dot emission. *Appl. Phys. Lett.* **99**, 41102; 10.1063/1.3615051 (2011).
9. Sapienza, L., Davanço, M., Badolato, A. & Srinivasan, K. Nanoscale optical positioning of single quantum dots for bright and pure single-photon emission. *Nat Commun* **6**, 7833; 10.1038/ncomms8833 (2015).
10. Moczala-Dusanowska, M. *et al.* Strain-Tunable Single-Photon Source Based on a Circular Bragg Grating Cavity with Embedded Quantum Dots. *ACS Photonics* **7**, 3474–3480; 10.1021/acsp Photonics.0c01465 (2020).
11. Liu, J. *et al.* A solid-state source of strongly entangled photon pairs with high brightness and indistinguishability. *Nat. Nanotechnol.* **14**, 586–593; 10.1038/s41565-019-0435-9 (2019).
12. Dousse, A. *et al.* Ultrabright source of entangled photon pairs. *Nature* **466**, 217–220; 10.1038/nature09148 (2010).
13. Warburton *et al.* Optical emission from a charge-tunable quantum ring. *Nature* **405**, 926–929; 10.1038/35016030 (2000).
14. Schall, J. *et al.* Bright Electrically Controllable Quantum-Dot-Molecule Devices Fabricated by In Situ Electron-Beam Lithography. *Adv Quantum Tech* **4**, 2100002; 10.1002/qute.202100002 (2021).
15. Singh, H. *et al.* Optical transparency induced by a largely Purcell-enhanced quantum dot in a polarization-degenerate cavity, 26.11.2021. arXiv:2111.13653v3

16. Fano, U. Effects of Configuration Interaction on Intensities and Phase Shifts. *Phys. Rev.* **124**, 1866–1878; 10.1103/PhysRev.124.1866 (1961).
17. Galli, M. *et al.* Light scattering and Fano resonances in high-Q photonic crystal nanocavities. *Appl. Phys. Lett.* **94**, 71101; 10.1063/1.3080683 (2009).
18. Limonov, M. F., Rybin, M. V., Poddubny, A. N. & Kivshar, Y. S. Fano resonances in photonics. *Nature Photon* **11**, 543–554; 10.1038/nphoton.2017.142 (2017).
19. Wang, H. *et al.* Towards optimal single-photon sources from polarized microcavities. *Nature Photon* **13**, 770–775; 10.1038/s41566-019-0494-3 (2019).